Magnetic Resonance Imaging 58 (2019) 44–55

Contents lists available at ScienceDirect

Magnetic Resonance Imaging

journal homepage: www.elsevier.com/locate/mri

Original contribution

Space-time variant weighted regularization in compressed sensing cardiac cine MRI

Alejandro Godino-Moya[a,*], Javier Royuela-del-Val[a], Muhammad Usman[b], Rosa-María Menchón-Lara[a], Marcos Martín-Fernández[a], Claudia Prieto[c], Carlos Alberola-López[a]

[a] Laboratorio de Procesado de Imagen, Department of Teoría de la Señal y Comunicaciones e Ingeniería Telemática, ETSIT, Universidad de Valladolid, Campus Miguel Delibes s.n., Valladolid 47011, Spain
[b] Department of Computer Science, University College London, London, United Kingdom
[c] King's College London, School of Biomedical Engineering and Imaging Sciences, London, United Kingdom

ARTICLE INFO

Keywords:
Space-time variant regularization
Cine cardiac MRI
Compressed sensing
k-t SPARSE-SENSE

ABSTRACT

Purpose: To analyze the impact on image quality and motion fidelity of a motion-weighted space-time variant regularization term in compressed sensing cardiac cine MRI.
Methods: k-t SPARSE-SENSE with temporal total variation (tTV) is used as the base reconstruction algorithm. Motion in the dynamic image is estimated by means of a robust registration technique for non-rigid motion. The resulting deformation fields are used to leverage the regularization term. The results are compared with standard k-t SPARSE-SENSE with tTV regularization as well as with an improved version of this algorithm that makes use of tTV and temporal Fast Fourier Transform regularization in x-f domain.
Results: The proposed method with space-time variant regularization provides higher motion fidelity and image quality than the two previously reported methods. Difference images between undersampled reconstruction and fully sampled reference images show less systematic errors with the proposed approach.
Conclusions: Usage of a space-time variant regularization offers reconstructions with better image quality than the state of the art approaches used for comparison.

1. Introduction

Cardiac disorders represent nowadays the first cause of death worldwide [1]. Cardiac cine MRI is considered the gold standard procedure for non-invasive evaluation of the cardiac function and anatomy [2], because of its high tissue contrast and its adequate spatial and temporal resolution [3]. Usually 2D cine MRI is performed with several slices covering the whole heart volume and data are acquired during consecutive breath-holds (BH) to prevent respiratory motion artifacts. Typically, one or two slices are acquired per BH, making this approach inefficient in time. Besides, patient cooperation is required and misalignment between slices may occur due to the difficulty of having equal states of apnea. Therefore, there is an on-going effort in the community to develop alternative methods that give rise to solutions that are both more time-efficient and more comfortable for the patient.

In the last years, multiple approaches have been proposed in order to reduce the acquisition times that are needed to perform a complete cine MRI study [4]. Compressed sensing (CS) has been successfully used in MRI reconstruction [5,6]. These methods make use of the redundancy that naturally exists in both spatial and temporal dimensions of the images, so that an image can be reconstructed from only a fraction of the whole k-space [2,7,8]. Temporal sparsity is often used for dynamic MRI [9], but the temporal regularization may affect negatively the dynamic properties of the moving regions of the image if the regularization parameter is not carefully selected; specifically, a low value of the regularization parameter produces aliasing artifacts due to k-space undersampling, whereas a high value of the regularization parameter produces temporal blurring artifacts and a loss of movement. It should be pointed out that not only structure fidelity should be preserved but also movement, so that motion abnormalities can be evaluated. In [2] a 2D pseudo-random eightfold accelerated method in Cartesian k-t space is described. The authors propose a model with two different sparsifying transforms, accounting for both dynamic and static regions in the image; specifically, they propose a combination of temporal total variation (tTV) for the dynamic region of the image, and temporal Fast Fourier Transform (FFT) to help suppress residual aliasing artifacts from static regions. However, these two regularization terms are applied globally to the whole image and the particular properties in terms of motion of the different regions of the image are not exploited. In [10], the authors take

* Corresponding author.
E-mail address: agodino@lpi.tel.uva.es (A. Godino-Moya).

https://doi.org/10.1016/j.mri.2019.01.005
Received 5 June 2018; Received in revised form 2 December 2018; Accepted 5 January 2019

into account the motion present in the images to promote sparsity in the solution, so that they can achieve further acceleration factors for the same image quality after reconstruction.

2D Free breathing approaches can reduce scan times and eliminate the need for BH. To deal with cardiac and breath motion, gated approaches have been proposed [11–13]. These techniques rely on surrogate signals for monitoring cardiac and respiratory cycles and data acquisition is usually performed in a specific time window (usually end expiration). Because of this, long setup times and calibration are needed and also efficiency in data acquisition decays. XD-GRASP [14] has been successfully applied to 2D free breathing cine. This approach does not limit data acquisition to some specific respiratory states; data are continuously acquired following radial trajectories in k-space without respiratory gating. Cardiac and respiratory signals can be acquired simultaneously or estimated directly from the acquired data. These two signals are then used to bin the data into multiple respiratory and cardiac states according to the cardiac phase and breathing position at which data were acquired. Images are afterwards reconstructed using CS algorithms imposing spatio-temporal smoothness constraints.

Multi-slice 2D cine approaches have the disadvantage of anisotropic spatial resolution. This leads to acquisitions that need to be done in a specific geometry (for instance, short-axis and four chambers among others), which requires a previous planning stage. 3D cine drops the need to acquire data in a specific geometry due to isotropic resolution, so that images can be reconstructed in any orientation. However, this technique is even more challenging since comparatively longer scan times are needed to meet demands of temporal and spatial resolutions, and volumetric coverage. Some techniques have been proposed to acquire the whole 3D volume in a single BH [15,16]. However, either spatial or temporal resolution has to be sacrificed because of the slow nature of MRI process. Nevertheless, [17] has recently achieved 3D reconstructions in a single BH with good resolution and image quality, although BH were relatively long (~20 s).

Other approaches have been proposed for free-breathing 3D; G-CASPR [18] defines a self-gated method that uses spiral profile ordering with tiny golden angle step in which reconstruction is preformed using iterative SENSE with tTV. ROCK [19] proposes a rotating Cartesian with golden angle ordering method where reconstruction is performed by using a joint parallel imaging and compressed sensing method with both spatial and temporal regularization. In [20] the authors extend the idea of XD-GRASP to reconstruct a 5D motion-resolved image series, where the five dimensions include the three spatial dimensions and two distinct temporal dimensions that represent cardiac and respiratory phases, respectively. Motion compensation has been incorporated [10,21] in a similar reconstruction pipeline to improve final image quality. Other approaches include low rank solutions for free-breathing, such as [22]. They rely on the assumption that cardiac motion can be separated from respiratory motion by splitting the image into a low rank component, which includes periodic background motion, and a sparse component, that includes respiratory motion. Thus, the problem is formulated by means of a cost function with a data fidelity term together with three different regularization terms: the low-rankness of one matrix, the sparsity of the second one and the sparsity of the motion corrected low-rank component.

Trajectories with denser sampling in the center of k-space such as radial [23,24] and spiral [25] have become popular for self-navigation approaches, since they provide more incoherent undersampling artifacts. In addition, radial imaging acquisition techniques show some advantages regarding motion properties [26]. However, these techniques are computationally demanding since gridding has to be performed in each iteration of the reconstruction process. Therefore, different approaches that use Cartesian trajectories with spiral profiles and golden angle step have been proposed. For instance, G-CASPR [27] is characterized by a scheme with uniform k-space sampling pattern and it is usually applied to static MRI, although it has also been used in cardiac cine [18] as indicated above. Nevertheless, compressed sensing shows better results if the center of k-space is sampled more densely [7,28]. On the other hand, VDRad [29] and ROCK [19] –among others– propose Cartesian k-space reordering methods, which are characterized by a variable sampling density where the center k-space is sampled more often than the periphery; the price to pay is a decrease of spectral efficiency, since some positions in the k-space are repeatedly acquired.

In this work, we propose a methodology to dynamically adapt the regularization parameter according to the presence of motion in each point of the image, based on a robust registration technique for non-rigid motion estimation, so that local properties in terms of motion of the image can be adequately exploited. Our purpose in this present paper, however, has been to analyze the impact of adaptive regularization, so motion information has been applied exclusively to this end, i.e., we use motion for reconstruction improvement while maintaining robustness to model mismatch. Using a regularization parameter as a function of motion favors dynamic behavior but does not bias the reconstruction to include spurious motion when the actual motion is incorrectly estimated. We compare our method with the formulation of k-t SPARSE-SENSE using tTV as sparsifying transform in the regularization term and with the formulation described in [2] which makes use of two such terms (namely, tTV and temporal FFT). For the 2D case, a Cartesian sampling scheme has been used. For the 3D case, however, we also define a general Cartesian sampling scheme with golden angle ordering that comprises, by means of a continuous parameter, both uniform sampling pattern and a pattern with dense sampling in the center of k-space as extreme cases, as well as all the intermediate sampling solutions. This enables us to test the conditions under which intermediate configurations may offer better performance for 3D cine cardiac MRI in terms of motion preservation, Cartesian sampling and spectral efficiency. Since these k-space visiting schemes are fully sampled in one direction, images are reconstructed in a per slice basis.

2. Methods

2.1. Image reconstruction

Image reconstruction was performed using a modified version of k-t SPARSE-SENSE [8]. Following the ideas in [2], we have substituted the temporal FFT originally used by tTV as the sparsifying transform, since in [2] the authors report with it lower root mean square error (RMSE) and higher temporal fidelity of myocardial wall motion with respect to the image of reference:

$$\hat{\boldsymbol{m}} = \arg\min_{\boldsymbol{m}} \; \|\boldsymbol{AFSm} - \boldsymbol{y}\|_{\ell_2}^2 + \lambda \, \|\nabla_t \boldsymbol{m}\|_{\ell_1} \tag{1}$$

where $\boldsymbol{y}$ is the acquired data in k-space, $\boldsymbol{m}$ is the image to be reconstructed, ∇_t is the tTV operator, $\boldsymbol{F}$ is the regular spatial FFT, $\boldsymbol{S}$ is the coil sensitivity profile matrix and $\boldsymbol{A}$ the sampling matrix. tTV is used as the sparsifying transform. However, our final formulation also introduces the space-time varying regularization parameter:

$$\hat{\boldsymbol{m}} = \arg\min_{\boldsymbol{m}} \; \|\boldsymbol{AFSm} - \boldsymbol{y}\|_{\ell_2}^2 + \lambda \, \|\boldsymbol{W}\nabla_t \boldsymbol{m}\|_{\ell_1} \tag{2}$$

where $\boldsymbol{W}$ is a diagonal weighting matrix that locally leverages the regularization parameter λ. This optimization problem is solved using the NESTA optimization algorithm [30]. Selection of λ and the entries of the weighting matrix are explained in the subsequent sections.

As previously stated, our methodology will be compared with k-t SPARSE-SENSE with tTV as sparsifying transform as well as with a version of this method with two regularization terms [2]. The latter incorporates an additional temporal FFT regularization term, the purpose of which is to suppress residual aliasing artifacts from static regions; specifically, the objective function is defined by:

$$\hat{\boldsymbol{m}} = \arg\min_{\boldsymbol{m}} \; \|\boldsymbol{AFSm} - \boldsymbol{y}\|_{\ell_2}^2 + \lambda_1 \, \|\nabla_t \boldsymbol{m}\|_{\ell_1} + \lambda_2 \, \|\boldsymbol{F}^t \boldsymbol{m}\|_{\ell_1} \tag{3}$$

where $\boldsymbol{F}^t$ is the temporal FFT. This method will be hereafter referred to as double sparsifying (DS), i.e., DS-k-t SPARSE-SENSE.

2.2. Motion estimation

The cardiac motion present in the images is estimated by using a groupwise registration method based on a B-spline deformation model [31], parameterized by the set of control points $\boldsymbol{\Theta}$, with the variance of the intensity along time as groupwise registration metric. The control points that minimize the value of the registration metric are found by solving the following optimization problem:

$$\underset{\boldsymbol{\Theta}}{minimize} \left\| \sum_{n=1}^{N} \left(\mathscr{T}_{\boldsymbol{\Theta},n} \boldsymbol{m}_n - \frac{1}{N} \sum_{k=1}^{N} \mathscr{T}_{\boldsymbol{\Theta},k} \boldsymbol{m}_k \right) \right\|^2 + R(\boldsymbol{\Theta}) \tag{4}$$

where $\mathscr{T}_{\boldsymbol{\Theta},n}$ represents the spatial deformation controlled by the set of parameters $\boldsymbol{\Theta}$, incurred by time frame n of the dynamic image $\boldsymbol{m}$ to match a common reference motion state. $R(\Theta)$ represents an additional regularization term given by the first/second order spatio-temporal derivatives of the motion fields, the purpose of which is to promote smoothness of the estimated spatial deformations [10]. Eq. (4) is solved by using of a nonlinear conjugate gradient algorithm. The value of $\boldsymbol{m}$ used to solve this equation is obtained by solving Eq. (1).

2.3. Definition of the weighting matrix

Different alternatives are studied to define the matrix $\boldsymbol{W}$ that appears in Eq. (2) and are described in the following subsections:

2.3.1. Plateau

We depart from a mask that contains the heart; this mask was defined as the largest region the temporal variance of which is higher than a certain threshold value γ; this value has been empirically selected to accommodate the whole heart in the datasets used.

Then, two different λ-values were defined, namely, λ_{static} for the outer region of the mask (background, i.e., static or pseudo-static area), and $\lambda_{dynamic}$ for the inner region of the mask (heart area). The procedure is formally expressed as

$$w_{plateau}(\boldsymbol{x}n) = \begin{cases} \lambda_{static}, & \mathrm{Var}(\boldsymbol{x}) < \gamma \\ \lambda_{dynamic}, & \mathrm{Var}(\boldsymbol{x}) \geq \gamma \end{cases} \tag{5}$$

with $w_{plateau}(\boldsymbol{x},n)$ the entry of matrix $\boldsymbol{W}$ corresponding to spatial position $\boldsymbol{x}$ and cardiac phase n, and the variance at point $\boldsymbol{x}$ is defined as

$$\mathrm{Var}(\boldsymbol{x}) = \frac{1}{N} \sum_{n=1}^{N} \left(m_n(\boldsymbol{x}) - \frac{1}{N} \sum_{k=1}^{N} m_k(\boldsymbol{x}) \right)^2 \tag{6}$$

The value of λ_{static} was set equal to λ_{opt} described in Appendix A. Since, as described in the Appendix, λ_{static} has been set as a function of the Signal to Error Ratio (SER), as this measure does not specifically reveal motion preservation, the complete set of reconstructions was revised by an experienced observer and $\lambda_{dynamic}$ was empirically set to $\lambda_{static}/3.51$ in order to maximize motion fidelity. Finally, the mask was low-pass filtered in order to have soft transitions between inner and outer regions.

2.3.2. Motion-weighted λ

As indicated in Section 2.2, motion is estimated by means of a first reconstruction; this reconstruction is obtained by applying Eq. (1). The resulting 2D deformation fields are used to leverage the regularization parameter in a second step of reconstruction by defining the entries of matrix $\boldsymbol{W}$ as

$$w_{disp}^{-1}(\boldsymbol{x},n) = \|\mathscr{T}_{\boldsymbol{\Theta},n}(\boldsymbol{x})\|^2 \tag{7}$$

The rationale of this action is to increase regularization in more static areas and to decrease in those areas where deformation is more pronounced. Alternatively, we have also used the velocity fields derived from the latter to define $\boldsymbol{W}$, i.e.,

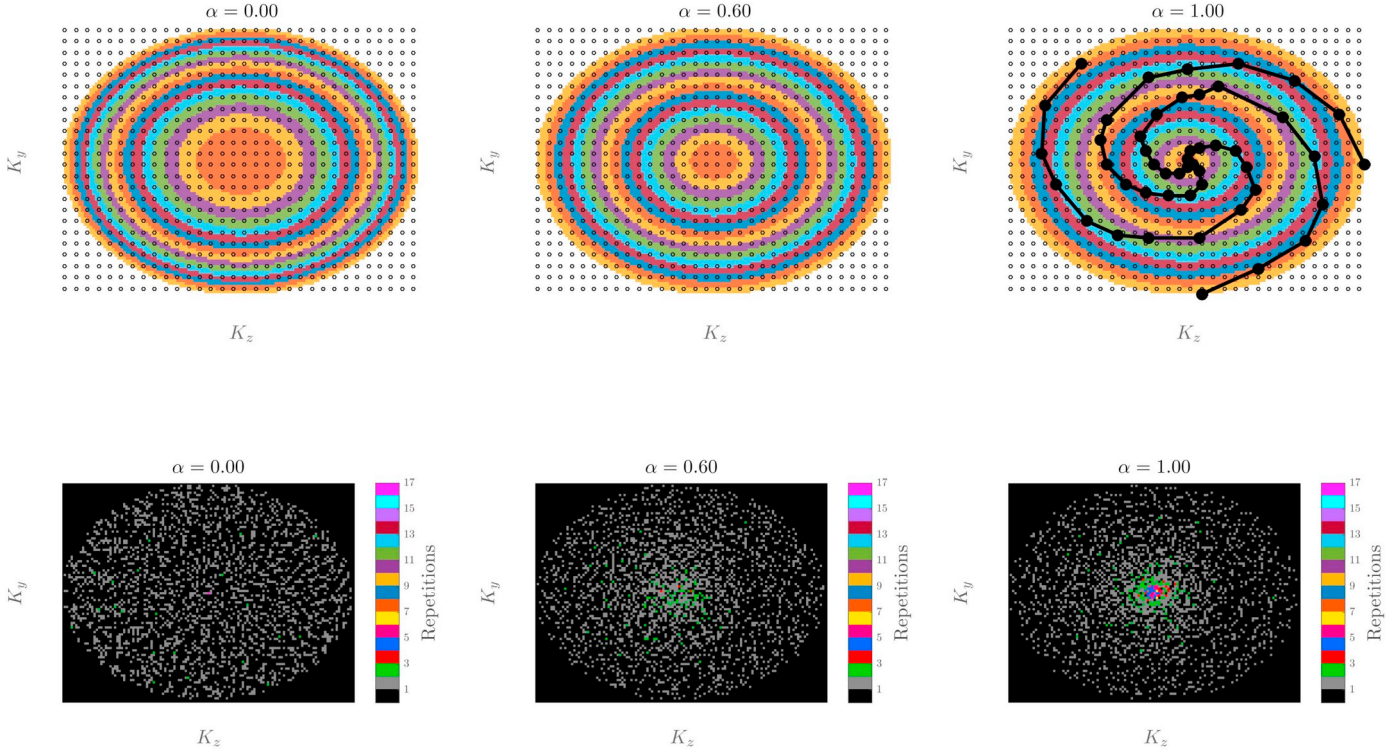

Fig. 1. proposed sampling pattern overview. Top line: on the left, each ring has the same area ($\alpha = 0.00$), on the right each ring has the same radial width ($\alpha = 1.00$). In the center an intermediate case is shown ($\alpha = 0.60$) where each ring has variable radial width and area. Bottom line: Resulting sampling patterns for different values of α after the cardiac binning. Sampling patterns show uniformity for $\alpha = 0.00$, although there are some zones with a few samples in the center of k-space. The density in the center of k-space increases progressively with the value of α and so do the repetitions of samples. The number of times that a sample has been visited is represented by colors. (For interpretation of the references to color in this figure legend, the reader is referred to the web version of this article.)

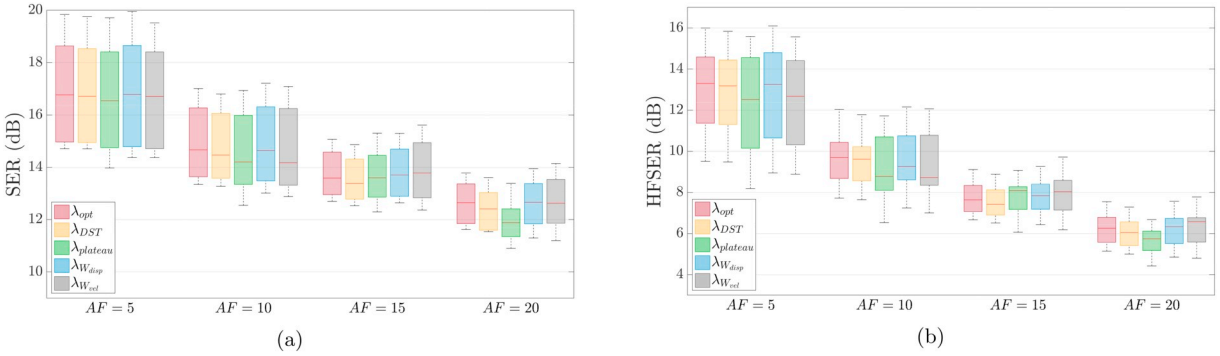

Fig. 2. SER (a) and HFSER (b) values of all reconstructions on 2D datasets for the five regularization strategies (λ_{opt}: k-t SPARSE-SENSE with tTV, λ_{DST}: DS-k-t SPARSE-SENSE, $\lambda_{plateau}$: plateau strategy, $\lambda_{W_{disp}}$: weighted λ by displacement fields, $\lambda_{W_{vel}}$: weighted λ by velocity fields), using Cartesian subsampling and different values AF.

$$w_{vel}^{-1}(\boldsymbol{x}, n) = \|\mathscr{T}_{\boldsymbol{\Theta},n}(\boldsymbol{x}) - \mathscr{T}_{\boldsymbol{\Theta},n+1}(\boldsymbol{x})\|^2 \quad (8)$$

In both cases the value of the resulting λ was limited to lie within the interval (λ_{static},$\lambda_{dynamic}$) to eliminate artifacts caused by improper motion estimation. It should be pointed out that 3D images are reconstructed in a per-slice basis, since the k-space visiting schemes are fully sampled in one direction, so 2D displacement fields have been used in both 2D and 3D experiments.

2.4. Sampling scheme

2.4.1. 2D sampling scheme

2D Cartesian fully sampled data were retrospectively undersampled using a Gaussian variable-density random undersampling pattern along the phase encoding direction [32] with different values of acceleration factor (AF).

2.4.2. 3D sampling scheme

A 3D Cartesian scheme is being used to avoid gridding operations. These sampling scheme is defined here as a general Cartesian sampling scheme with spiral ordering of samples and golden-angle step.

Table 1
EF values (mean value ± standard deviation) calculated in the 2D reconstructions using all the regularization strategies (λ_{opt}: k-t SPARSE-SENSE with tTV, λ_{DST}: DS-k-t SPARSE-SENSE, $\lambda_{plateau}$: plateau strategy, $\lambda_{W_{disp}}$: weighted λ by displacement fields, $\lambda_{W_{vel}}$: weighted λ by velocity fields) for $AF = 5$ and $AF = 10$. The EF reference value, calculated in the fully sampled image, is shown for comparison. *p*-Values between EF calculated in fully sampled image and reconstructed images are also shown. *p*-Values below the significance level 0.05 are boldfaced.

Strategy	$AF = 5$		$AF = 10$	
	EF	*p*-Value	EF	*p*-Value
λ_{opt}	60.21 ± 2.92	0.1282	55.02 ± 4.65	**0.0006**
λ_{DST}	60.27 ± 4.16	0.1282	52.36 ± 5.63	**0.0006**
$\lambda_{plateau}$	62.46 ± 4.97	0.6200	57.00 ± 3.69	**0.0041**
$\lambda_{W_{disp}}$	59.97 ± 5.19	0.2593	57.60 ± 4.70	**0.0175**
$\lambda_{W_{vel}}$	61.69 ± 4.08	0.3829	57.67 ± 4.44	**0.0262**
Reference	64.35 ± 4.87			

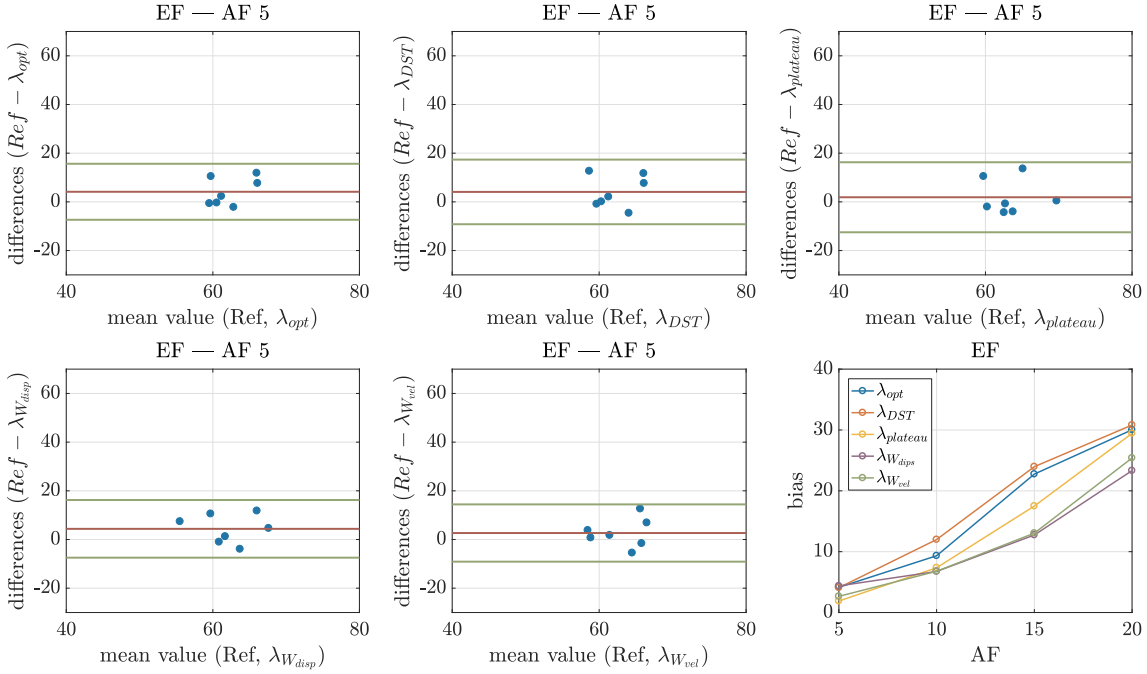

Fig. 3. Bland-Altman plots for ejection fraction (EF) for all the regularization strategies (λ_{opt}: k-t SPARSE-SENSE with tTV, λ_{DST}: DS-k-t SPARSE-SENSE, $\lambda_{plateau}$: plateau strategy, $\lambda_{W_{disp}}$: weighted λ by displacement fields, $\lambda_{W_{vel}}$: weighted λ by velocity fields) on 2D datasets using Cartesian trajectories and $AF = 5$. The observed bias is also represented parameterized by the parameter AF.

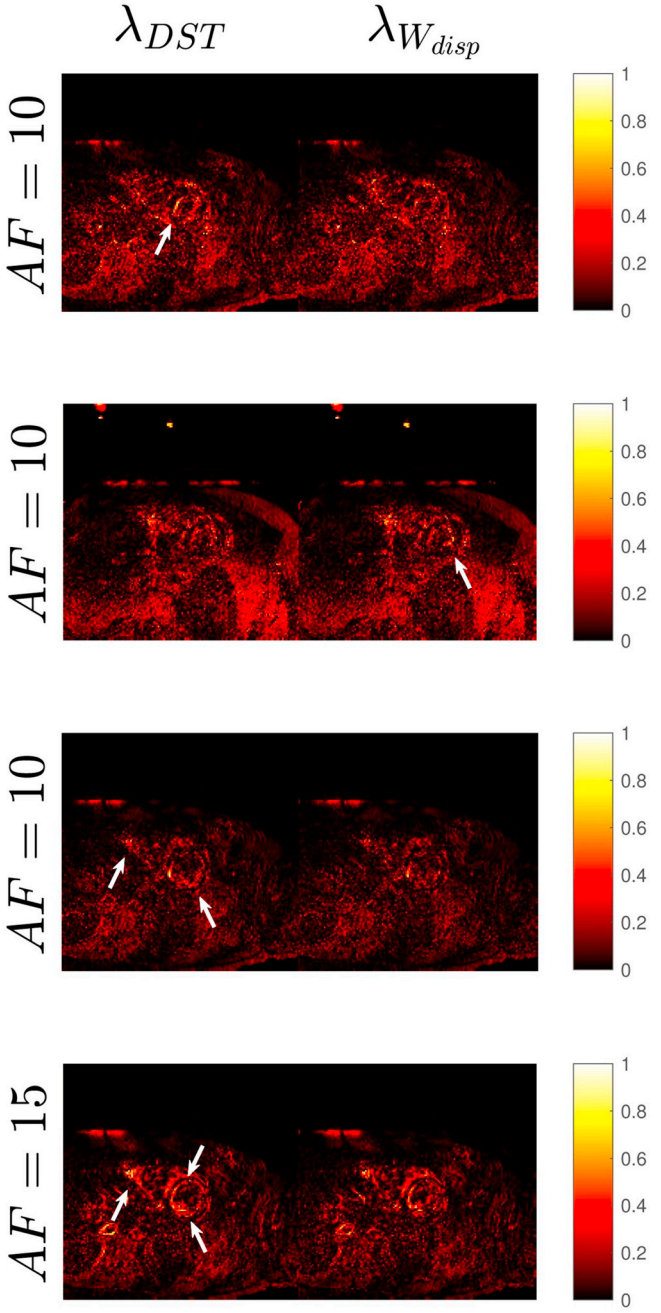

Fig. 4. Normalized error images between reference and reconstructions on 2D datasets with different values of AF (first to third rows: $AF = 10$, last row: $AF = 15$) using DS-k-t SPARSE-SENSE (λ_{DST}) and weighted λ by displacement fields ($\lambda_{W_{disp}}$) strategies. White arrows point at significant locations where error is higher.

Specifically, samples are acquired from the center to the periphery of the (K_y, K_z)-plane, giving rise to spiral-like trajectories (see Fig. 1); K_x dimension is fully sampled. Given a spiral length L, the (K_y, K_z)-plane is divided into L concentric elliptic rings (no corners are used) and each ring in turn is divided in L sectors. The radii of every ring along the K_y and K_z directions (R_{K_y} and R_{K_z}, respectively) are controlled by the parameter α, as shown in Eq. (9)

$$\left.\begin{aligned} R_{K_y}(k) &= \alpha \cdot \frac{kN}{2L} + (1-\alpha)\cdot \frac{N}{2}\sqrt{\frac{k}{L}} \\ R_{K_z}(k) &= \alpha \cdot \frac{kM}{2L} + (1-\alpha)\cdot \frac{M}{2}\sqrt{\frac{k}{L}} \end{aligned}\right\} \tag{9}$$

where $N \times M$ is the size of the image, $k = 1, 2, \ldots, L$ and $0 \le \alpha \le 1$.

It is easy to check that a value of α equal to zero produces rings with constant area while a value of α equal to one produces rings with constant radial width but with increasing area when moving to the periphery of the k-space. Since each sector will be sampled an equal number of times, the case $\alpha = 0$ yields uniform sampling of the k-space, while in the case $\alpha = 1$ the sampling density decreases at the periphery. Thus, the parameter α enables the selection from a uniform —or quasi-uniform— sampling pattern of k-space to a denser sampling in its center.

The samples within each ring are ordered first by radius and second by angle in the k-space. Afterwards, trajectories are formed by choosing each time one sample of one ring and sector forming a spiral twist (for example, $(\text{sector}, \text{ring}) = (l, l)$, $1 \le l \le L$, then $(\text{sector}, \text{ring}) = (l, l+1)$, $1 \le l \le L-1$ and so forth). Finally, the resulting trajectories are ordered according to the golden angle (137.5°). The number of total acquired samples is adjusted by the desired AF.

3. Experiments

3.1. 2D experiments

2D Cartesian, fully sampled dynamic cine BH gated acquisitions were performed on 7 healthy subjects in a 1.5 T Philips scanner with a bSSFP sequence. Some relevant parameters of the acquisitions include flip-angle 60°, TR/TE = 3/1.5 ms, spatial resolution $2 \times 2\,\text{mm}^2$, slice thickness 8 mm, 20 cardiac phases, FOV $320 \times 320\,\text{mm}^2$.

3.2. 3D experiments

A 2.2 mm isotropic 3D + t cardiac MR scan was performed on five swine in a 3 T Philips scanner with volumetric bTFE sequence. Some relevant parameters of the acquisition include flip-angle 30°, TR/TE = 1.95/0.976 ms, 20 cardiac phases. Reconstructed voxel size was $1.417 \times 1.417 \times 1.1\,\text{mm}^3$. Acquisitions were cardiac-triggered by means of a PPU unit located at the swine's tail. Due to the physiology of these animals, respiratory motion in sedated pigs is barely appreciated and causes no artifacts, so the acquisition did not make use of any additional hardware to deal with breathing issues.

3.3. Overview of the experiments

The 2D datasets were retrospectively subsampled with the procedure described in [32] for different values of AF, whereas 3D datasets were retrospectively subsampled with the procedure described in Section 2.4, with different values of AF and α. Complex Gaussian noise has also been added to these datasets in k-space with different values of the standard deviation to analyze the effect of noise in the reconstruction.

Images have been reconstructed with the two versions of k-t SPARSE-SENSE (Eqs. (1) and (3)) and with the three different approaches of weighted regularization described before (plateau, weighted λ by displacement fields and weighted λ by velocity fields, respectively, Eqs. (5), (7) and (8)). Both signal to error ratio (SER) and high frequency signal to error ratio (HFSER) [33] were calculated as image quality measurements. SER and HFSER are defined as Eqs. (10) and (11), respectively

$$SER = 10 \cdot log\left(\frac{||\,\boldsymbol{m}^{ref}\,||^2}{||\,\boldsymbol{m}^{ref} - \boldsymbol{m}^{rec}\,||^2}\right) \tag{10}$$

$$HFSER = 10 \cdot \log\left(\frac{||\,\text{LoG}(\boldsymbol{m}^{ref})\,||^2}{||\,\text{LoG}(\boldsymbol{m}^{ref}) - \text{LoG}(\boldsymbol{m}^{rec})\,||^2}\right) \tag{11}$$

where $\boldsymbol{m}^{ref}$ is the fully sampled image (reference), $\boldsymbol{m}^{rec}$ is the reconstructed image, and LoG is a Laplacian of Gaussian filter that captures boundaries, with a kernel size of 7×7 pixels and standard deviation of 1.5.

For 2D experiments, we have also obtained quantitative cardiac function indicators, namely, end diastolic volume (EDV), end systolic

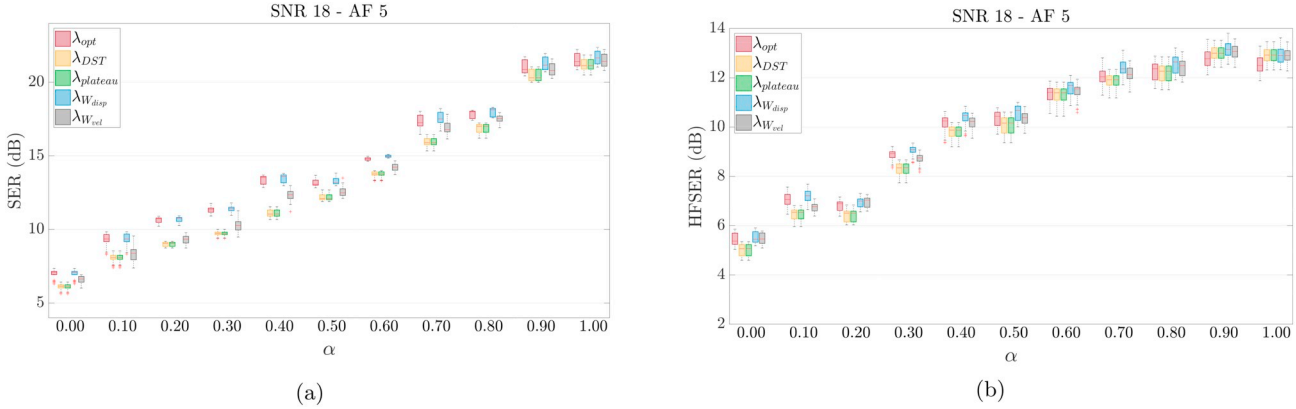

Fig. 5. SER (a) and HFSER (b) values for all reconstructions on 3D datasets for the five regularization strategies (λ_{opt}: k-t SPARSE-SENSE with tTV, λ_{DST}: DS-k-t SPARSE-SENSE, $\lambda_{plateau}$: plateau strategy, $\lambda_{W_{disp}}$: weighted λ by displacement fields, $\lambda_{W_{vel}}$: weighted λ by velocity fields) using different values of α and $AF = 5$ and $SNR = 18$ dB.

volume (ESV), stroke volume (SV) and ejection fraction (EF). EDV and ESV were computed using Simpson's rule and manual segmentation with an in-house software for all the reconstructions using all regularization strategies. Afterwards, SV and EF were calculated as:

$$SV = EDV - ESV \tag{12}$$

$$EF = 100 \cdot \frac{SV}{EDV} \tag{13}$$

Since this paper is focused on the importance of regularization, the selection of the parameter λ has received special attention. We have resorted to a methodology based on cross validation [34]. The details of the procedure are described exhaustively in Appendix A, where two parameters (namely, the total number of datasets used in the cross validation procedure, K, and the number of datasets used for the training group, P) have to be set. In our case, we have chosen $K = 7$ and $P = 4$ for 2D experiments and $K = 5$ and $P = 4$ for the 3D experiments. As for the methods in Eqs. (1) and (3) that we compare with, the parameters have been set $\lambda_1 = \lambda_{opt}$ and $\lambda_2 = \lambda_1/10$ following the same criteria as in [2].

4. Results

4.1. 2D results

Fig. 2 show boxplots of SER and HFSER parameterized by AF for all the reconstructions using the five regularization strategies on the 2D datasets using Cartesian trajectories. Mann-Whitney U tests have been conducted between SER and HFSER distributions for reconstructions with $AF = 20$; no significant differences were found.

Table 2
p-Values of SER distributions for reconstructions on 3D datasets using all regularization strategies (λ_{opt}: k-t SPARSE-SENSE with tTV, λ_{DST}: DS-k-t SPARSE-SENSE, $\lambda_{plateau}$: plateau strategy, $\lambda_{W_{disp}}$: weighted λ by displacement fields, $\lambda_{W_{vel}}$: weighted λ by velocity fields) with $AF = 20$ and (a) $\alpha = 0.7$ and (b) $\alpha = 1$. p-Values below the significance level 0.05 are boldfaced.

	λ_{opt}	λ_{DST}	$\lambda_{plateau}$	$\lambda_{W_{disp}}$
(a)				
λ_{DST}	**0.0000**			
$\lambda_{plateau}$	**0.0000**	1.0000		
$\lambda_{W_{disp}}$	0.0877	**0.0000**	**0.0000**	
$\lambda_{W_{vel}}$	**0.0000**	**0.0056**	**0.0056**	**0.0000**
(b)				
λ_{DST}	**0.0000**			
$\lambda_{plateau}$	**0.0000**	1.0000		
$\lambda_{W_{disp}}$	0.3329	**0.0000**	**0.0000**	
$\lambda_{W_{vel}}$	**0.0000**	**0.0339**	**0.0339**	**0.0000**

Fig. 3 shows Bland-Altman plots of the EF calculated on the reconstructions using the five strategies of regularization. The resulting bias can be appraised as a function of AF. Mann-Whitney U tests were performed between the EF values of reference and EF values obtained by all regularization strategies. The resulting EF values (mean ± standard deviation) and their p-values are shown in Table 1 for two different values of AF.

Fig. 4 shows normalized error images for representative cases between reference and reconstructions on 2D datasets using two different regularization strategies (DS-k-t SPARSE-SENSE and weighted λ by displacement fields) and different values of AF (10 and 15).

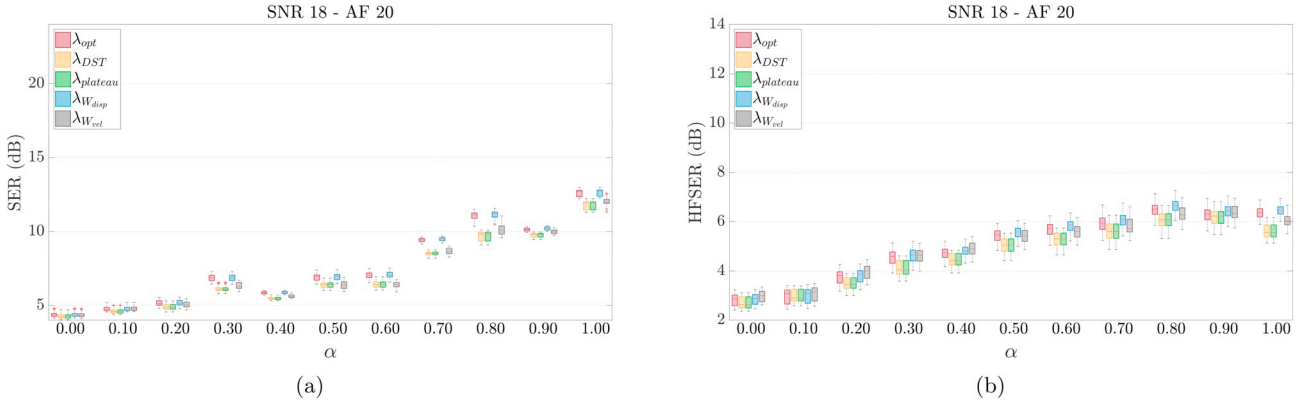

Fig. 6. SER (a) and HFSER (b) values for all reconstructions on 3D datasets for the five regularization strategies (λ_{opt}: k-t SPARSE-SENSE with tTV, λ_{DST}: DS-k-t SPARSE-SENSE, $\lambda_{plateau}$: plateau strategy, $\lambda_{W_{disp}}$: weighted λ by displacement fields, $\lambda_{W_{vel}}$: weighted λ by velocity fields) using different values of α and $AF = 20$ and $SNR = 18$ dB.

Table 3
p-Values of HFSER distributions for reconstructions on 3D datasets using all regularization strategies (λ_{opt}: k-t SPARSE-SENSE with tTV, λ_{DST}: DS-k-t SPARSE-SENSE, $\lambda_{plateau}$: plateau strategy, $\lambda_{W_{disp}}$: weighted λ by displacement fields, $\lambda_{W_{vel}}$: weighted λ by velocity fields) with $AF = 20$ and (a) $\alpha = 0.7$ and (b) $\alpha = 1$. *p*-Values below the significance level 0.05 are boldfaced.

	λ_{opt}	λ_{DST}	$\lambda_{plateau}$	$\lambda_{W_{disp}}$
(a)				
λ_{DST}	**0.0040**			
$\lambda_{plateau}$	**0.0040**	1.0000		
$\lambda_{W_{disp}}$	0.1120	**0.0000**	**0.0000**	
$\lambda_{W_{vel}}$	0.2707	**0.0351**	**0.0351**	**0.0199**
(b)				
λ_{DST}	**0.0000**			
$\lambda_{plateau}$	**0.0000**	1.0000		
$\lambda_{W_{disp}}$	0.1537	**0.0000**	**0.0000**	
$\lambda_{W_{vel}}$	**0.0000**	**0.0000**	**0.0000**	**0.0000**

4.2. 3D results

Figs. 5 and 6 show boxplots of SER and HFSER parameterized by α for all the reconstructions on the 3D datasets using the five regularization strategies for a selected value of SNR and $AF = 5$ and $AF = 20$, respectively.

Table 2 shows *p*-values from Mann-Whitney *U* tests (significance

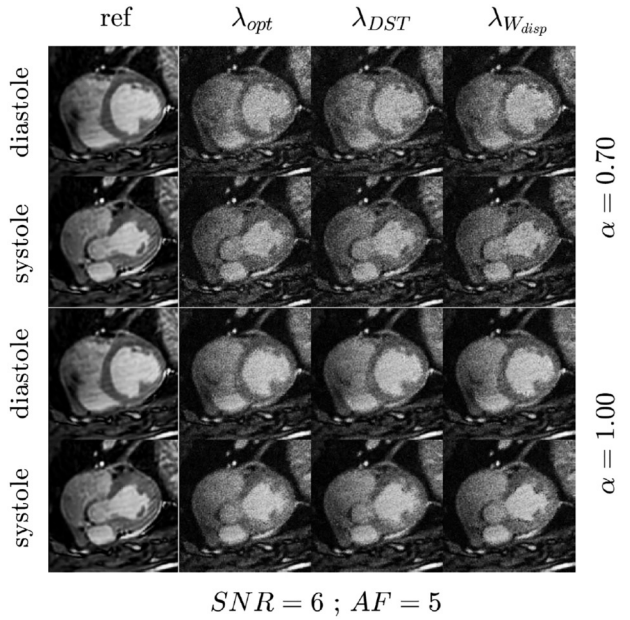

Fig. 8. Fully sampled image (ref) compared to reconstructions on 3D datasets with $AF = 5$ and two different values of α, using k-t SPARSE-SENSE with tTV (λ_{opt}), DS-k-t SPARSE-SENSE (λ_{DST}) and weighted λ by displacement fields ($\lambda_{W_{disp}}$) and $SNR = 6$.

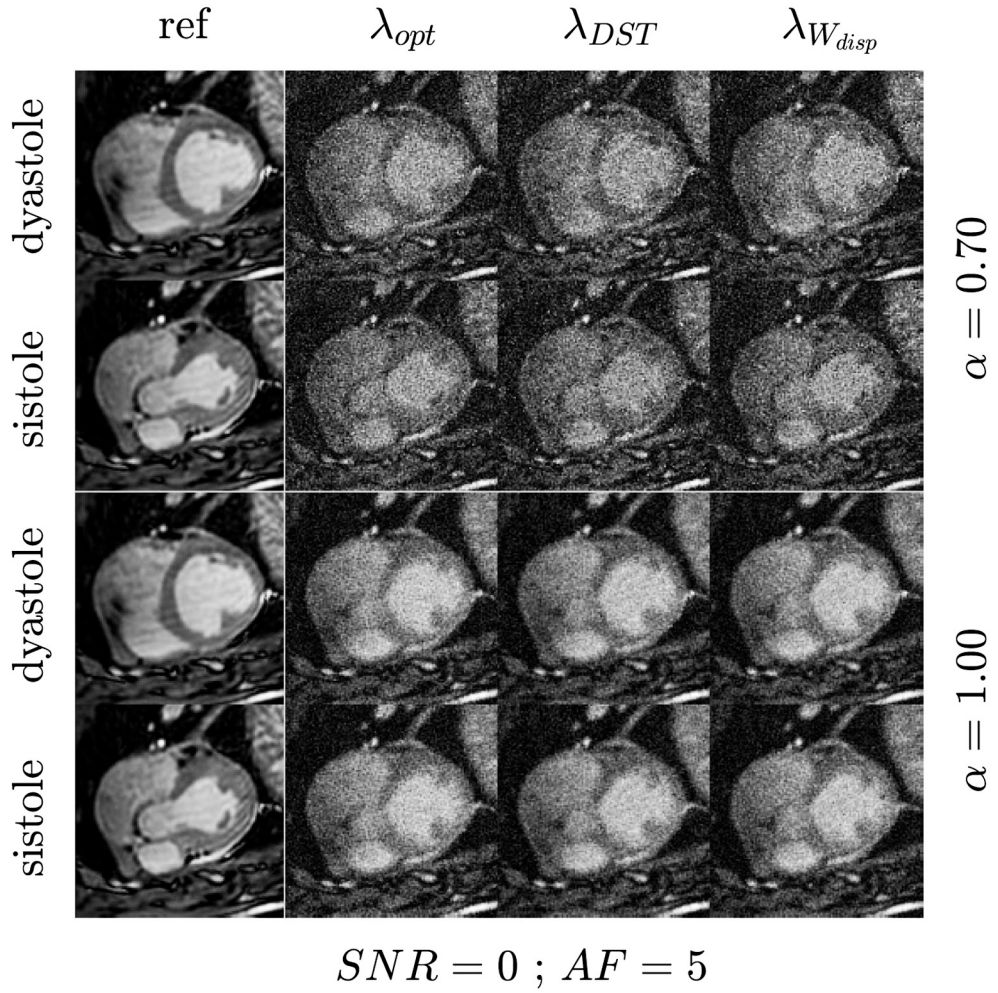

Fig. 7. Fully sampled image (ref) compared to reconstructions on 3D datasets with $AF = 5$ and two different values of α, using k-t SPARSE-SENSE with tTV (λ_{opt}), DS-k-t SPARSE-SENSE (λ_{DST}) and weighted λ by displacement fields ($\lambda_{W_{disp}}$) and $SNR = 0$.

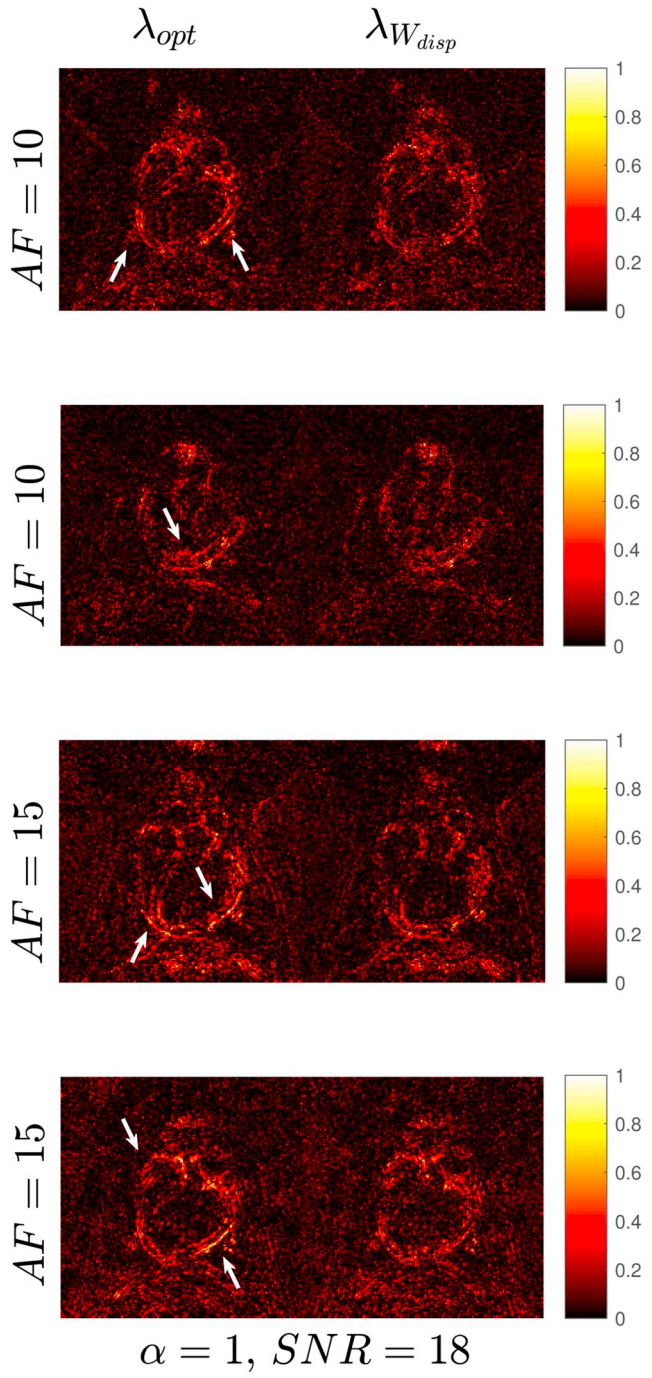

Fig. 9. Normalized error images between reference and reconstructions on 3D datasets with different values of AF (first and second rows: $AF = 10$, third and fourth rows: $AF = 15$) using k-t SPARSE-SENSE with tTV (λ_{opt}) and weighted λ by displacement fields ($\lambda_{W_{disp}}$) strategies, $\alpha = 1$ and $SNR = 18$. White arrows point at significant locations where error is higher.

level: $p = 0.05$) performed between SER distributions for reconstructions on 3D datasets using the five regularization strategies for $AF = 20$ and two values of α (0.7 and 1.0). In the same way, Table 3 shows p-values for HFSER distributions.

In Figs. 7 and 8 we show a comparison between reconstructions of the systole and the diastole time instants on 3D datasets for three different regularization strategies (k-t SPARSE-SENSE with tTV, DS-k-t SPARSE-SENSE and weighted λ by displacement fields), two different values of α (0.7 and 1), $AF = 5$ and with two low levels of SNR (0 and 6 dB, respectively). For simplicity, we only compare the weighted λ by displacement fields strategy with the other reported regularization strategies, since the former provides the best reconstructions (Figs. 5 and 6) in the motion-weighted strategies.

Fig. 9 shows normalized error images for representative cases between reference and reconstructions on 3D datasets using two different regularization strategies (k-t SPARSE-SENSE with tTV and weighted λ by displacement fields), $SNR = 18$, $\alpha = 1$ and different values of AF (10 and 15).

Video S1 in the supplementary material shows reconstructions for different regularization strategies for $SNR = 6$, $AF = 5$ and four values of α. Each row corresponds with a different value of α, specifically $\alpha = 0.7$, $\alpha = 0.8$, $\alpha = 0.9$ and $\alpha = 1$, from top to bottom. The fully sampled image is displayed on the leftmost column for comparison. The three following columns correspond respectively to reconstructions using k-t SPARSE-SENSE with tTV, DS-k-t SPARSE-SENSE and weighted λ by displacement fields. The next three columns correspond with error images between the fully sampled image and each reconstruction method. The last three columns correspond with total accumulated error for each reconstruction (see Fig. 10 for a clarification). Video S2 shows corresponding results for $SNR = 18$.

5. Discussion

Results on 2D experiments show that in terms of SER and HFSER (Fig. 2b) our motion-weighted regularization schemes provide higher figures for higher values of AF. Despite these differences are not statistically significant (at both $p < 0.05$ and $p < 0.01$) we indeed can observe some artifacts in the motion of papillary muscles, but this motion seems more natural in reconstructions using weighted λ by displacement fields (Eq. (7)). Error images shown in Fig. 4 reveal that the error is higher in the left-ventricle myocardium and in the apex.

Regarding functional measurements, Bland-Altman plots (Fig. 3) show agreement between measurements, but a bias in measurements can also be observed. Nevertheless, *p*-values in Table 1 reveal that there are not significant differences ($p > 0.05$) in EF between the reference value obtained in the fully sampled image and those obtained in reconstructions by using all the regularizations strategies when low values of AF are used. Significant differences ($p < 0.05$) appear when AF increases, although those space-time variant regularization strategies (namely, weighted λ by displacement fields and weighted λ by velocity fields) give rise to higher p-values which are not significant at a lower level value ($p < 0.01$).

The positive sign of the bias means that the regularization strategies provide lower values than those of the ground truth. This being the case, we can infer that there is a loss of movement in the reconstructed images; however, the figure shows that regularization strategies with variant parameter (and, specifically, that in Eq. (7)) preserve heart movement better than those with a single and/or invariant regularization parameter (Eqs. (1) and (3)).

The results on the 3D experiments data in Figs. 5 and 6 show that reconstructions with higher values of SER and HFSER are obtained when α is close to –albeit not necessarily equal to– 1. Differences between methods are more notable when AF increases. k-t SPARSE-SENSE with tTV and weighted λ by displacement fields regularization strategies give rise to reconstructions with higher SER and HFSER values than the other three regularization strategies. However, between these two strategies there are not significant differences in terms of SER and HFSER (Tables 2 and 3), which is a result that supports our method, since λ_{opt} was chosen, as described in the Appendix, to maximize SER, so the method with λ_{opt} is acting in this experiment as a SER benchmark. Nevertheless, it can be seen in supplementary Video S2 that weighted λ by displacement fields strategy produces reconstructions with more natural movement, especially in papillary muscles, than the other strategies. We have included, for easier reading, several examples in Fig. 9 that reveal higher and more structured error values in myocardium in k-t SPARSE-SENSE with tTV reconstructions than those

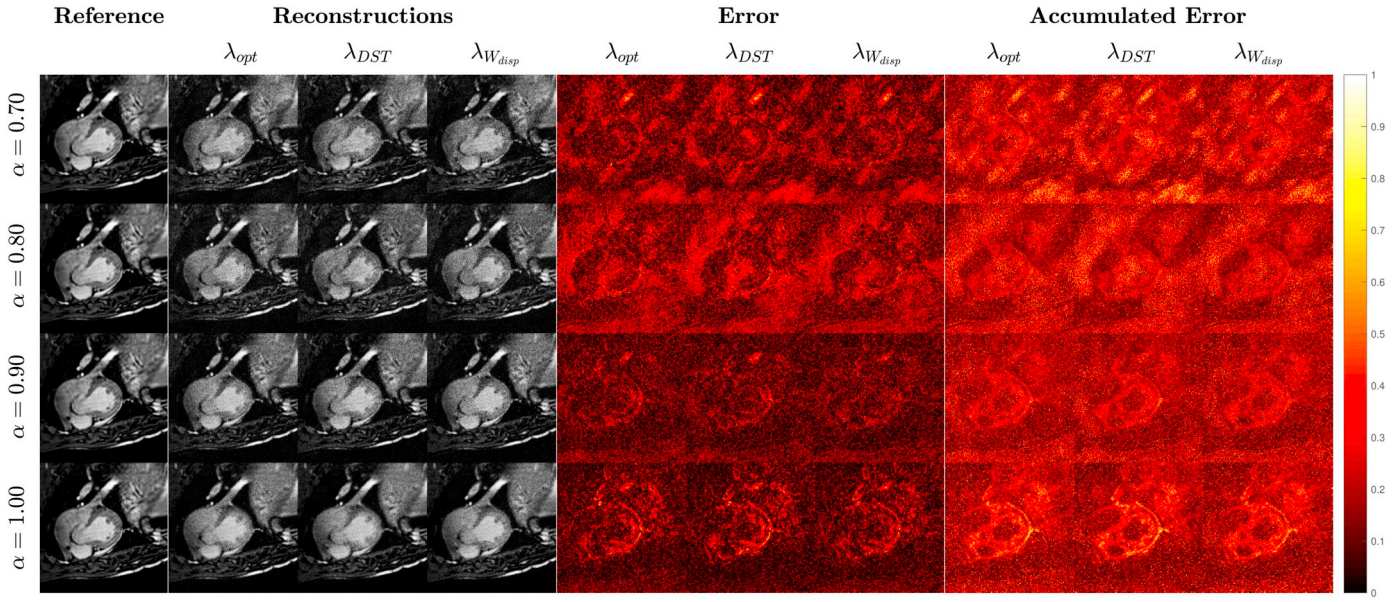

Fig. 10. Content of supplementary videos (λ_{opt}: k-t SPARSE-SENSE with tTV, λ_{DST}: DS-k-t SPARSE-SENSE, $\lambda_{W_{disp}}$: weighted λ by displacement fields).

using weighted λ by displacement fields. This result is in line with the fact that SER is limited when used to quantify image quality perception and, specially, to measure the amount of movement present in a dynamic image. Therefore, the selected optimal value λ_{opt} may be higher than necessary, so that images tend to be over-regularized. HFSER, on the other hand, does not seem to provide additional information to these experiments. As for the other three methods, they do show significant differences with respect to weighted λ by displacement fields which, again, supports our proposal.

These experiments also allowed us to study the effect of noise in the different regularization strategies. In Fig. 7 it can be observed that, for the same value of SNR and AF, reconstructed images with $\alpha = 1$ in systole and diastole are very similar to each other. However, reconstructed images with $\alpha = 0.7$ differ notably. Additionally, in Video S1 it can be observed that the reconstructed images with $\alpha = 1$ seem to show step-wise transitions while images with $\alpha = 0.7$ move seamlessly along the cardiac cycle; it can also be noticed that the accumulated error is more structured when $\alpha = 1$ than for $\alpha = 0.7$. In Video S2, with a higher SNR, differences are hardly appreciated in terms of quality of motion although the error images maintain a higher structure for $\alpha = 1$. This evidence highlights that $\alpha = 1$ gives rise to images with less natural movement in the presence of noise, even though they obtain higher SER and HFSER values. Thus, in low signal to noise ratio scenarios, it would be preferable to choose an intermediate value of α close to 0.7, since heart movement is better preserved and noise can be eliminated by using tailored techniques.

As mentioned before, the proposed method involves two steps: (1) initial reconstruction and (2) second reconstruction using a variant regularization term derived from the motion fields obtained from step (1). It is indeed more critical to have errors in step (1); at this step, errors arise due to either over- or under-regularization. The former gives rise to images with less artifacts (which is desirable) but more static (which is not desirable), while the latter is accompanied by more artifacts but better motion preservation. At step (2), artifacts may hinder motion estimation, but this estimation will never be correct if motion is lost at step (1). Therefore, it is critical not to over-regularize in step (1); under-regularization in step (1) may lead to worse motion estimates in step (2) but, since motion information is solely used to leverage temporal differences, the method would never introduce spurious movement, although it may give rise to non-optimal regularization in those specific areas where motion is incorrectly assessed. This sort of remaining artifacts, however, may be smoothed by tailored

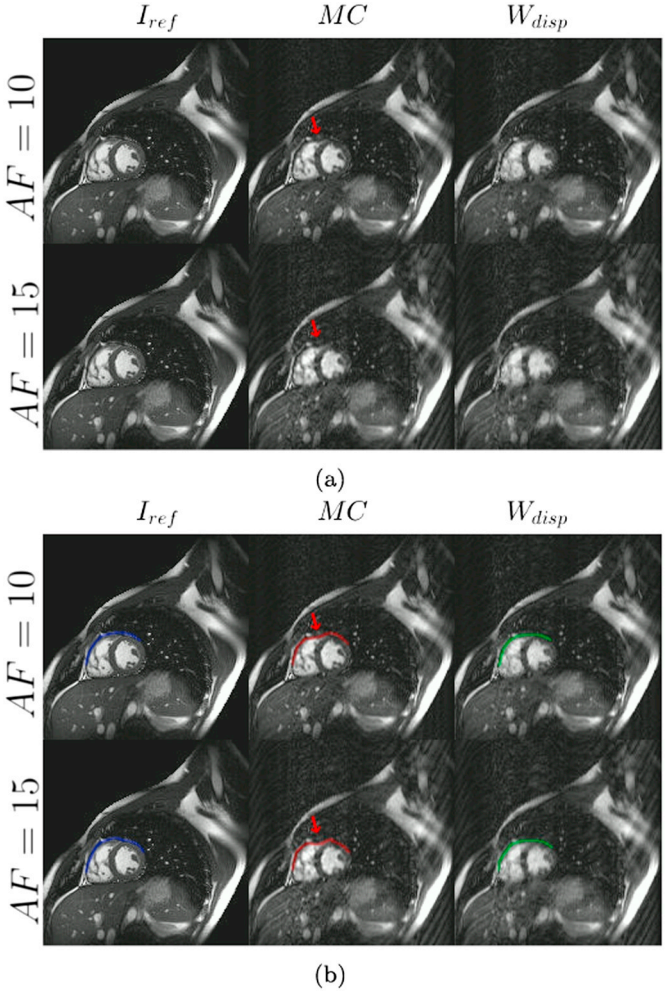

Fig. 11. Results on real data, using 2D Cartesian pseudorandom undersampling with acceleration factors (AF) of 10 (top row) and 15 (bottom row). Left column, fully sampled images of reference (I_{ref}); center column, reconstructed images using a motion compensation algorithm (MC); right column, reconstructed images using displacement fields to leverage the regularization parameter (W_{disp}). Red arrows point areas with spurious deformation. In (b) the same images as in (a) are represented, but the myocardium is marked with colored lines to highlight spurious deformations. (For interpretation of the references to color in this figure legend, the reader is referred to the web version of this article.)

techniques. Therefore, we point out the importance of the procedure to select the parameter λ and develop a method to select it automatically for the step (1).

The main limitation of using Eq. (7) is the need to estimate movement from a prior reconstruction, making the whole reconstruction process longer. However, the development of high performance implementations of the algorithms on graphics processing units (GPUs) drastically reduces these reconstructions times. As a matter of fact, we have incorporated this information in the reconstruction pipeline as well [10,21]; nevertheless, as previously stated, errors in motion field estimation may be propagated to the final reconstruction so robustness to this sort of mismatch is of importance. This may be the case in 2D imaging of the apical and basal slices, where structures come in and out of the planes along the cardiac cycle. To illustrate this, we have sampled one of the human images with a pseudorandom Cartesian scheme ($AF = 10$) and we have reconstructed them both with the motion-compensated method (MC) described in [10] and with the method here proposed. We can observe in Fig. 11a that the MC algorithm introduces spurious deformations in the lung/right ventricle area (pointed with arrows). Interestingly, the rounded shape of the right ventricle is preserved when $\lambda_{W_{disp}}$ algorithm is used instead. In Fig. 11b we have marked part of the myocardium with colored lines to highlight this fact. As observed, the method proposed in this paper seems more robust when model mismatches are observed.

According to this evidence, complementarity between these two methods is worth exploring. This could be done be by setting λ as a function of the residual motion observed in the (ideally) motion compensated images.

6. Conclusion

We have proposed a methodology to leverage the regularization parameter in compressed sensing reconstruction of dynamic cardiac images using displacement fields by means of motion estimation; therefore, regularization is spatially and temporally varying. We have compared our strategy with the k-t SPARSESENSE with tTV as well as with a subsequent version of it that uses two different regularization terms with tTV and temporal FFT (referred to in the paper as double-sparsifying k-t SPARSE-SENSE). We observed that our strategy provides better reconstructions in terms of motion fidelity.

We have also proposed a parameterized Cartesian sampling scheme that allows the practitioner to select from a uniform sampling pattern of k-space to a denser sampling scheme in its center by setting the value of the parameter α. For cine cardiac MRI α values in the vicinity of $\alpha = 1$ have been shown as preferable; however, higher noise content makes intermediate configurations ($\alpha \approx 0.7$) draw better results.

Supplementary data to this article can be found online at https://doi.org/10.1016/j.mri.2019.01.005.

Acknowledgments

The authors acknowledge funds from Ministerio de Economía y Competitividad, Spain, under Research Grants TEC2014-57428-R and TEC2017-82408-R and Junta de Castilla y León, Spain, under Grant VA069U16. The authors are also indebted to the Centro Nacional de Investigaciones Cardiovasculares (CNIC) for kindly providing the swine images.

Appendix A. Selection of the regularization parameter λ

The methodology we have followed to choose the regularization parameter is applied for each pair of (AF, α) used in the experiments. Specifically, we first define a set of twelve tentative values for λ, ranging from 10^{-4} to 1, equally spaced in a logarithmic scale. Let K denote the number of datasets available and let $k \in \{1, \ldots, K\}$. For each dataset k and each tentative value λ_i, $(1 \le i \le 12)$ we reconstruct the image and compute the signal to error ratio, $SER_k(\lambda_i)$ [see Eq. (A.1)], within a region containing the heart:

$$SER_k(\lambda_i) = 10 \cdot log\left(\frac{|| \boldsymbol{m}_k^{ref} ||^2}{|| \boldsymbol{m}_k^{ref} - \boldsymbol{m}_k^{ref}(\lambda_i) ||^2}\right) \tag{A.1}$$

where $\boldsymbol{m}_k^{ref}$ is the fully sampled image (reference) for dataset k and $\boldsymbol{m}_k^{ref}(\lambda_i)$ is the corresponding reconstructed image using the regularization parameter λ_i.

The λ_i that gave rise to the highest SER value is then selected for dataset k:

$$\lambda_k^{ds} = \arg\max_{\boldsymbol{i}} SER_k(\lambda_i) \tag{A.2}$$

Then, a cross validation method was used to determine the optimum value, i.e., λ_{opt}. This method can be described as follows (see Fig. A.12): The K datasets were divided into P training datasets and $K - P$ test datasets; we have been exhaustive in the number $\binom{K}{P}$ of different combinations to avoid any sort of bias. Let $\boldsymbol{c}_i$ denote the group of training datasets included in combination i $\left(1 \le i \le \binom{K}{P}\right)$ and let $c_{i,j}$ denote the index in the set $\{1, \ldots, K\}$ of the j-th element of $\boldsymbol{c}_i$ $(1 \le j \le P)$, i.e., $c_{i,j} \in \{1, \ldots, K\}$. For this j-th element we take its associated $\lambda_{c_{i,j}}^{ds}$ and we use it to reconstruct all other datasets in $\boldsymbol{c}_i$; then we calculate the accumulated SER ($aSER$):

$$aSER_{c_{i,j}} = \sum_{n=1, n \ne j}^{P} SER_{c_{i,n}}(\lambda_{c_{i,j}}^{ds}) \tag{A.3}$$

For each training group $\boldsymbol{c}_i$ we select the candidate $\lambda_{\boldsymbol{c}_i}^{test}$ by maximizing the accumulated SER within $\boldsymbol{c}_i$, i.e.,

$$\lambda_{\boldsymbol{c}_i}^{test} = \arg\max_{\boldsymbol{j}} aSER_{\boldsymbol{c}_{i,j}}(\lambda_{c_{i,j}}^{ds}) \tag{A.4}$$

The final step to determine λ_{opt} (for each pair (AF, α)) is to select the best $\lambda_{\boldsymbol{c}_i}^{test}$ with $1 \le i \le \binom{K}{P}$. Let $\boldsymbol{d}_i$ denote the group of datasets not included

in $\boldsymbol{c}_i$ (i.e., the testing datasets associated to the training set $\boldsymbol{c}_i$); correspondingly, let $d_{i,j}$ denote de index in the set $\{1, \ldots, K\}$ of the j-th element of $\boldsymbol{d}_i$ $(1 \leq j \leq K - P)$. We calculate the *aSER* as follows:

$$aSER^{test}(\lambda_{\boldsymbol{d}_i}^{test}) = \sum_{n=1}^{K-P} SER_{d_{i,n}}(\lambda_{\boldsymbol{d}_i}^{test}) \tag{A.5}$$

With these values $\boldsymbol{d}_i^{test}, \left(1 \leq i \leq \binom{K}{P}\right)$, we select the optimum value as

$$\lambda_{opt} = \arg\max_i aSER^{test}(\lambda_{\boldsymbol{d}_i}^{test}) \tag{A.6}$$

As indicated in Section 3.3, we have used $K = 5$ and $P = 4$ for the 3D datasets and $K = 7$ and $P = 4$ for 2D datasets.

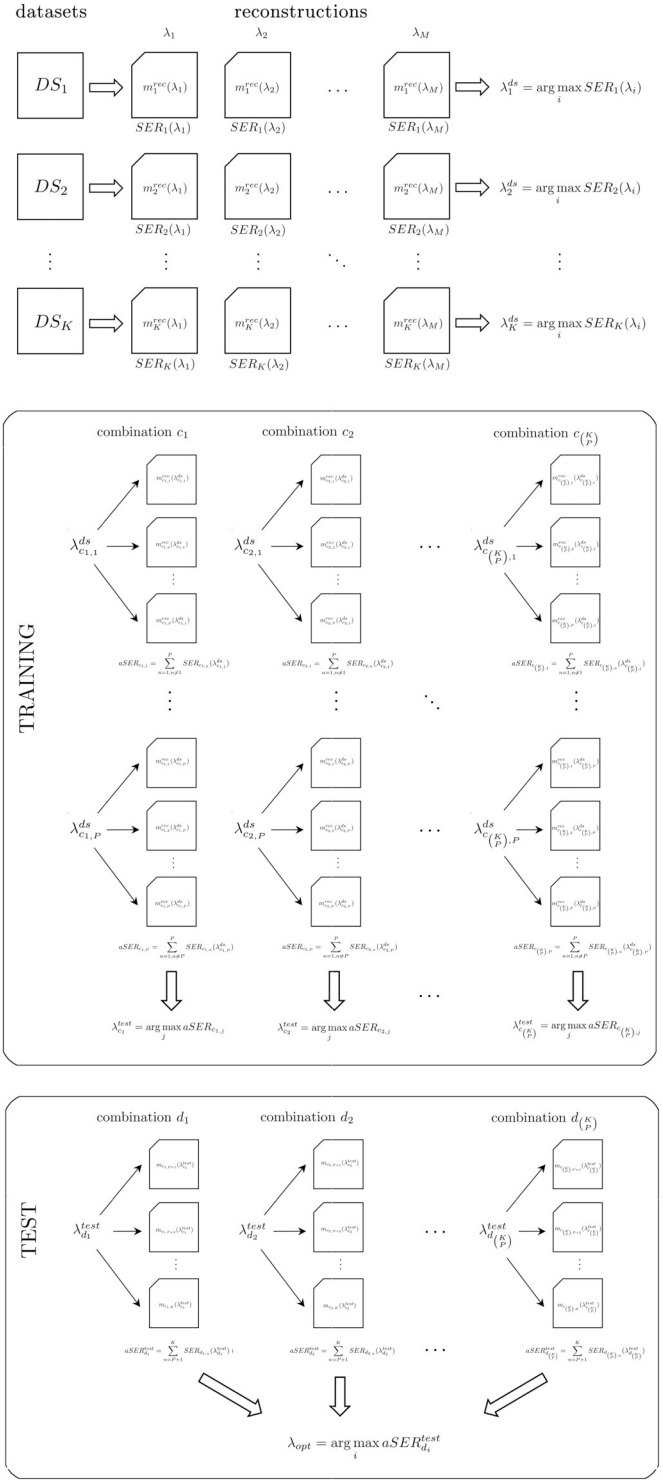

Fig. A.12. Lambda selection method overview.

References

[1] WHO. World Health Organization methods and data sources for country-level causes of death 2000–2015. Global health estimates technical paper. 2017. p. 1–81.
[2] Feng L, Srichai MB, Lim RP, Harrison A, King W, Adluru G, et al. Highly accelerated real-time cardiac cine MRI using k - t SPARSE-SENSE. Magn Reson Med 2013;70(1):64–74.
[3] Bogaert J, Dymarkowski S, Taylor AM, Muthurangu V. Clinical Cardiac MRI. vol. 2. Germany: Springer Verlag; 2012.
[4] Tsao J. Ultrafast imaging: principles, pitfalls, solutions, and applications. 2010;32(2):252–66.
[5] Candès EJ, Romberg J, Tao T. Robust uncertainty principles: exact signal reconstruction from highly incomplete frequency information. IEEE Trans Inf Theory 2006;52(2):489–509.
[6] Donoho DL. Compressed sensing. IEEE Trans Inf Theory 2006;52(4):1289–306.
[7] Lustig M, Donoho D, Pauly JM. Sparse MRI: the application of compressed sensing for rapid MR imaging. Magn Reson Med 2007;58(6):1182–95.
[8] Otazo R, Kim D, Axel L, Sodickson DK. Combination of compressed sensing and parallel imaging for highly accelerated first-pass cardiac perfusion MRI. Magn Reson Med 2010;64(3):767–76.
[9] Gamper U, Boesiger P, Kozerke S. Compressed sensing in dynamic MRI. Magn Reson Med 2008;59(2):365–73.
[10] Royuela-del-Val J, Cordero-Grande L, Simmross-Wattenberg F, Martín-Fernández M, Alberola-López C. Nonrigid groupwise registration for motion estimation and compensation in compressed sensing reconstruction of breath-hold cardiac cine MRI. Magn Reson Med 2015;75(4):1525–36.
[11] Yuan Q, Axel L, Hernandez EH, Dougherty L, Pilla JJ, Scott CH, et al. Cardiac-respiratory gating method for magnetic resonance imaging of the heart. Magn Reson Med 2000;43(2):314–8.
[12] Peters DC, Nezafat R, Holger E, Stehning C, Manning WJ. 2D free-breathing dual navigator-gated cardiac function validated against the 2D breath-hold acquisition. J Magn Reson Imaging 2008;28(3):773–7.
[13] Usman M, Atkinson D, Heathfield E, Greil G, Schaeffter T, Prieto C. Whole left ventricular functional assessment from two minutes free breathing multi-slice CINE acquisition. Phys Med Biol 2015;60(7):N93–107.
[14] Feng L, Axel L, Chandarana H, Block KT, Sodickson DK, Otazo R. XD-GRASP: golden-angle radial MRI with reconstruction of extra motion-state dimensions using compressed sensing. Magn Reson Med 2016;75(2):775–88.
[15] Mascarenhas NB, Muthupillai R, Cheong B, Pereyra M, Flamm SD. Fast 3D cine steady-state free precession imaging with sensitivity encoding for assessment of left ventricular function in a single breath-hold. 2006;187(5):1235–9.
[16] Jeong D, Schiebler ML, Lai P, Wang K, Vigen KK, François CJ. Single breath hold 3D cardiac cine MRI using kat-ARC: preliminary results at 1.5 T. Int J Cardiovasc Imaging 2015;31(4):851–7.
[17] Wetzl J, Schmidt M, Pontana F, Longère B, Lugauer F, Maier A, et al. Single-breath-hold 3-D CINE imaging of the left ventricle using Cartesian sampling. Magn Reson Mater Phys Biol Med 2018;31(1):19–31.
[18] Usman M, Ruijsink B, Nazir MS, Cruz G, Prieto C. Free breathing whole-heart 3D CINE MRI with self-gated Cartesian trajectory. Magn Reson Imaging 2017;38:129–37.
[19] Fei H, Ziwu Z, Minsong C, Yingli Y, Ke S, Peng H. Respiratory motion resolved, self-gated 4d-mri using rotating Cartesian k-space (rock). Med Phys 2017;44(4):1359–68.
[20] Feng L, Coppo S, Piccini D, Yerly J, Lim RP, Masci PG, et al. 5D whole-heart sparse MRI. Magn Reson Med 2017;79(2):826–38.
[21] Menchón-Lara RM, Royuela-delVal J, Godino-Moya A, Cordero-Grande L, Simmross-Wattenberg F, Martín-Fernández M, et al. An efficient multi-resolution reconstruction scheme with motion compensation for 5D free-breathing whole-heart MRI. Vol. 10555 LNCS of lecture notes in computer science. Germany: Springer Verlag; 2017. p. 136–45.
[22] Tolouee A, Alirezaie J, Babyn P. Nonrigid motion compensation in compressed sensing reconstruction of cardiac cine MRI. Magn Reson Imaging 2018;46:114–20.
[23] Schäffter T, Volker R, Carlsen IC. Motion compensated projection reconstruction. Magn Reson Med 1999;41(5):954–63.
[24] Larson AC, White RD, Laub G, McVeigh ER, Li D, Simonetti OP. Self-gated cardiac cine MRI. Magn Reson Med 2004;51(1):93–102.
[25] Liu C, Bammer R, Kim DH, Moseley ME. Self-navigated interleaved spiral (SNAILS): application to high-resolution diffusion tensor imaging. Magn Reson Med 2004;52(6):1388–96.
[26] Feng L, Grimm R, Block KT, Chandarana H, Kim S, Xu J, et al. Golden-angle radial sparse parallel MRI: combination of compressed sensing, parallel imaging, and golden-angle radial sampling for fast and flexible dynamic volumetric MRI. Magn Reson Med 2014;72(3):707–17.
[27] Prieto C, Doneva M, Usman M, Henningsson M, Greil G, Schaeffter T, et al. Highly e_cient respiratory motion compensated free breathing coronary MRA using golden-step Cartesian acquisition. J Magn Reson Imaging 2015;41(3):738–46.
[28] Adcock B, Hansen A, Roman B, Teschke G. Generalized sampling: stable reconstructions, inverse problems and compressed sensing over the continuum. Adv Imaging Electron Phys 2014;182:187–279.
[29] Cheng JY, Zhang T, Ruangwattanapaisarn N, Alley MT, Uecker M, Pauly JM, et al. Free-breathing pediatric MRI with non-rigid motion correction and acceleration. J Magn Reson Imaging 2015;42(2):407–20.
[30] Becker S, Bobin J, Candès EJ. NESTA: a fast and accurate first-order method for sparse recovery. SIAM J Imaging Sci 2011;4(1):1–39.
[31] Rueckert D, Sonoda LI, Hayes C, Hill DLG, Leach MO, Hawkes DJ. Non-rigid registration using free-form deformations: application to breast MR images. Med Imaging IEEE Trans 1999;18(8):712–21.
[32] Salman AM, Lei H, Marijn B, Justin R. Motion-adaptive spatiotemporal regularization for accelerated dynamic MRI. Magn Reson Med 2013;70(3):800–12.
[33] Cruz G, Atkinson D, Buerger C, Schae_ter T, Prieto C. Accelerated motion corrected three-dimensional abdominal MRI using total variation regularized SENSE reconstruction. Magn Reson Med 2016;75(4):1484–98.
[34] Hastie T, Tibshirani R, Friedman J. The elements of statistical learning. vol. 2. New York, NY, USA: Springer New York Inc.; 2001.